Supporting Information for Millennial-scale climate oscillations triggered by deglacial meltwater discharge in last glacial maximum simulations

Yvan M. Romé[1], Ruza F. Ivanovic[1], Lauren J. Gregoire[1], Sam Sherriff-Tadano[1], Paul J. Valdes[2]

[1]School of Earth and Environment, University of Leeds, Leeds, UK

[2]School of Geographical Sciences, University of Bristol, Bristol, UK

Contents of this file

March 24, 2022, 8:41pm

Introduction

The supporting information presented here contains eight sections and ten figures as supplements to the main text. This includes details on the last glacial maximum boundary conditions (section S1, Figure S1), the meltwater discharge protocol (section S2, figure S2), the global mean salinity correction algorithm (section S3), the smoothing bathymetry algorithm (section S4, Figures S3, S4, S5), the spectral analysis algorithm (section S5), the definition of warm and cold composite modes (section S6, Figures S6, S7, S8), the definition of the intertropical convergence zone index (section S7), the definition of the centre of mass (section S8), the definition of the average zones (Figures S9 and the mixed layer depth anomalies over the composite warm modes (Figures S10).

S1. Simulating the Last Glacial Maximum

For atmospheric trace gases, we adopted Last Glacial macimum (LGM) values of 190 ppm for CO_2 (Bereiter et al., 2015), 375 ppb for CH_4 (Loulergue et al., 2008), and a slightly lower concentration of 193 ppb for N_2O (compared to 200 ppb in the protocol) (Schilt et al., 2010), which corresponds to the 21 ka BP point in the interpolation between transient records of ice cores (Ivanovic et al., 2016). For the ice sheets, and associated fields, ice sheet extent, surface elevation and the resulting land-sea mask and ocean bathymetry were all derived from the GLAC-1D ice sheet reconstruction (Tarasov & Peltier, 2002; Tarasov et al., 2012; Briggs et al., 2014; Ivanovic et al., 2016) at year 21 ka BP. The ice sheet geometries (Figure S1) and associated palaeogeographical fields were not modified at any time of any simulations. The GLAC-1D reconstruction contains patches of ice over central Siberia and southern sectors of the Rocky Mountains (e.g. Tarasov et al., 2012) that can reach up to 100 m thick. Because they correspond to regions where the fractional ice mask is less than 0.5 (Ivanovic et al., 2016), these were not considered nor discussed further in this study.

The remaining parameters were set to the values indicated in Kageyama et al. (2017), including radiative forcing from insolation and dust.

S2. Meltwater discharge protocol

The algorithm used to create the meltwater discharge input was adapted from Ivanovic, Gregoire, Wickert, Valdes, and Burke (2017). At each 100-years time step and for each spatial grid cell where ice is present, ice elevation changes were converted into a freshwater-equivalent flux. To avoid generating strong peaks during the transformation of discrete snapshots of ice sheet geometry into a continuous time series, the flux was smoothed by taking the average of two consecutive time steps. Because we do not have a physically robust way to displace freshwater from the ocean back to the ice sheet, only ice losses were taken into account, ice accumulation being subsequently turned to zero. These steps can be summarised by equation S1, where $flux$ ($kg\,m^{-2}\,s^{-1}$) is the mass flux at a grid cell, $hice$ (m) the ice elevation at the same grid cell, $\rho = 1000\,kg\,m^{-3}$ water density, n represents the time step and $\Delta t = 100\,yrs$ the interval between two time steps.

$$flux_n = max(0, \rho \frac{hice_{n+1} - hice_n}{\Delta t}) \tag{S1}$$

Next, the 100-years time-step series was linearly interpolated into an annual series. The fluxes were then routed to an ocean cell following a global drainage network map consistent with GLAC-1D topography, using the routing coordinates provided with the PMIP4 last deglaciation protocol (Ivanovic et al., 2016). To be consistent with our model, this scattered discharge pattern was remapped to the coarser HadCM3 ocean grid, ensuring that the meltwater reaches the ocean by redistributing any routing points overlapping the land mask to their closest ocean cell.

Because the ocean model is a rigid-lid model (Gordon et al., 2000), oceanic freshwater forcing (including runoff, ice melting, precipitation/evaporation) is prescribed as virtual salinity fluxes. One possible consequence of this parameterisation is that large fluxes can lead to some grid cells being capped at 0 PSU (minimum salinity) in the case of large freshwater inputs. This can be problematic, since we would approach the limits of the equation of state (Bryan & Cox, 1972; Fofonoff & Millard Jr, 1983; Fofonoff, 1985), and would prevent the full freshwater forcing from being applied to the ocean during episodes of rapid, voluminous meltwater discharge. Instead of trying to estimate when the salinity saturation may be reached, we adopt a cautious approach by reproducing and updating the spreading algorithm employed by Ivanovic, Gregoire, Burke, et al. (2018) and Ivanovic, Gregoire, Wickert, and Burke (2018). This algorithm collects all the freshwater from its grid-cell point of entry to the ocean, and spreads it uniformly at the surface of neighbouring discharge regions of at least 500 m depth. The new version of the algorithm used here only modifies the definition of some spreading regions and collection boxes in accordance with the new inputs (i.e. the old algorithm would have missed some of the new meltwater fluxes as a new ice sheet and palaeogeography is being applied in accordance with GLAC-1D; the previous studies follow ICE-6G_C). These areas are plotted in Figure S2*b*. It is possible, although rare, that some discharge grid cells may not be caught by the spreading protocol. We checked at each time step that the residual's signal did not exceed 0.1% of the initial flux, a value we consider small enough to be thought of as noise.

Tests for a previous study (Ivanovic, Gregoire, Burke, et al., 2018) showed that there was a negligible difference between the results simulated using point-source or more distributed

meltwater patterns during the Heinrich Stadial period, and although these freshwater fluxes are different (the previous study used the ICE-6G_C ice sheet history), they are of sufficiently similar rate/amplitude that we are confident that a similar inference applies to the new simulations presented here, whilst also ensuring that we avoid hitting the 0 PSU lower cap (see above).

The resulting fluxes, including the signal in key regions, are plotted in Figure S2*a*. Note the difference in this figure panel between smaller collection boxes (bold contours offshore), larger spreading regions (constituent coloured boxes), and key regions (colours) considered for plotting the fluxes (e.g. as time series in Figure S2*a*). Snapshots in time of the meltwater distribution are shown by Figure S2*c*.

Once the meltwater input file was created, we added the contribution of the river and iceberg run-off that was calculated to close the hydrological cycle during the Pre-Industrial. Note that meteoric runoff routing follows the configuration calculated when producing the HadCM3 PMIP4 LGM palaeogeography.

S3. Global mean salinity target

In multi-millennial simulations on the scale presented here, long-term drifts in global mean salinity can arise under equilibrium climate forcings due to internal imbalances in snowfall/melt and iceberg calving (which is prescribed and therefore cannot vary dynamically), and evaporation/precipitation over inland seas, which are not hydrologically connected to the ocean. To conserve water in the model and avoid these long-term drifts, we apply a method for keeping global mean salinity constant that distributes any required correction across the whole volume of the ocean. This approach was preferred to a surface correction, because the latter has a greater propensity for inducing surface salinity drifts that impact large scale ocean circulation, as concluded by Dentith, Ivanovic, Gregoire, Tindall, and Smith (2019). The method applied for this study is the VFLUX method described fully by Dentith et al. (2019). At each ocean model time step, global mean salinity is corrected so that the global mean salinity hits the prescribed target in accordance with the terrestrial ice volume and global ocean volume at that timestep with respect to the pre-industrial. The target is calculated following equation S2, where sal_{target} $(g\,kg^{-1})$ is the global salinity target of the experiment, $sal_{ref} = 34.83\,g\,kg^{-1}$ is the reference HadCM3 salinity at 0 ka, V_{ocn} (m^3) is the ocean volume at 0 ka BP and ΔV_{ice} (m^3) is the difference in ice volume between 0 ka BP and the current timestep of the simulation. Thus, even though the LGM ice sheet layout (i.e. as prescribed to the atmosphere model) stays constant in our experiments, the effects of changes in terrestrial ice volume on global mean ocean salinity are taken into account through the global salinity target. Thus, each simulation has a global mean salinity target that corresponds exactly with the ice sheet

configuration at the time of the meltwater snapshot (Table 1), with the *CTRL* target set to $35.8334\,g\,kg^{-1}$.

$$sal_{target} = sal_{ref} * \frac{V_{ocn}}{V_{ocn} + \Delta V_{ice}} \tag{S2}$$

S4. Smoothing bathymetry algorithm

After a few thousand years of integration, five out of the seven simulations (*CTRL*, *21.5k*, *21k*, *19.4k*, *18.2k*) presented in this article crashed because of a stream function instability in the Philippines Sea. This instability takes the form of a dipole where two grid cells reach unsustainable high/low barotropic stream function values; for example, as shown for *CTRL* in Figure S3. A week (model time) before the crash, the instability is undetectable. When the pattern appears, it gets out of control in less than a simulated day. The precise cause of this crash is not known, but it always occurs at the same location and it appears to be related to the complex bathymetry of the region.

In order to tackle this issue, we restarted the runs having smoothed the bathymetry of the Philippines and South China Seas (Figure S4*f*). Because we cannot exactly determine the inception of the instability, we restarted the simulations a few model years/decades before the crashes: *CTRL* at year 2,800, *21.5k* at year 3,060, *21k* at year 2,650, *19.4k* at year 8,610 and *17.8k* at year 8,900. The same smoothing was applied to all simulations and all the other boundary conditions remain unchanged. After this one intervention, all experiments successfully ran to completion.

Small disruptions of the climate are induced by the smoothing and restart process. For example, there is a slight increase of long-term drifts in *CTRL* (Figure S5), probably caused by a slight perturbation to the equilibrium state from introducing a small amount of noise at the restart alongside the smoothing of South China Sea and Indonesian bathymetry; the model is adjusting to the minor modifications. However, the trends are of the same order of magnitude as in the previous two and a half thousand years of simula-

tion, and significantly smaller than during the last one thousand years of spin-up, implying that climate remains close to its equilibrium state. Similar changes in the long term drifts are seen in *21.5k* and *21k* (not shown), but are impossible to assess for *19.4k* and *17.8k* because of their oscillatory variability. Nonetheless, any impact of the smoothing and restart on the oscillations is imperceptible if it is exists at all. After the introduction of the smoothed dumps (arrows in Figure 3*b*), there is no significant change of behaviour in any of the time series. We cannot determine conclusively whether the smoothing influences the periodicity of the oscillations. However, the climate and ocean behaviours at the end of the restarted simulations are consistent with the variability observed before the smoothing.

Here, we show the spatial response induced by the change of bathymetry for *CTRL* only (Figure S4), but all the other simulations were analysed and returned comparable results. The resulting smoothed bathymetry has the greatest impact on the surface air temperatures, sea surface temperatures and sea surface salinity in the Philippines Sea and the Sea of Japan, with changes of up to 7°C, 8°C and 5 $g\,kg^{-1}$ respectively, but only in grid cells very local to the bathymetric modifications. Outside of these cells, the effect is either very small or statistically insignificant. In particular, we do not see any significant response from the climate system in the North Atlantic, which is the primary domain of interest for this study. In conclusion, we infer that the modifications induced by smoothing South China Sea and Indonesian bathymetry mid-run are minor and do not impact the main findings of the study.

S5. Spectral analysis of the oscillating simulations

Averaging model outputs over time, whether it is by using running means or taking snapshots, is a useful tool for assessing the main trends of a simulation. The downside is that we lose information on the dynamics and variability that are shorter/faster or of comparable duration to the length of the averaging period. Because our aim is to focus on millennial-scale variability only, we here propose a method based on spectral analysis.

Fourier theory, implemented in the Scilab Python project, allows for calculating the harmonics and the Power Spectral Density (PSD) of a time series. By applying that method to the simulated time series of Greenland temperatures at the NGRIP site, we derive a spectrum for each *oscillating* and *slow-recovery* simulations in 4*c*. Note that the mean value of the signals were subtracted before calculating the PSD to compensate the offset from the fixed component (at 0 Hz). The amplitude of the harmonics corresponds to the most significant frequencies in the time series' signals. The frequencies of millennial-scale variability peak around $10^{-3}\,yrs^{-1}$ (corresponding to a period of $1000\,yrs$), while the frequencies associated with inter-annual variability are higher around $1\,yrs^{-1}$. In *oscillating simulations*, we do indeed observe a clear dominant periodicity of about a thousand years, which corresponds to frequencies previously estimated from Figure 3. On the other hand, *18.2k* does not display such a significant peak in the Fourier space and cannot, therefore, be considered as quasi-oscillating. In order to only conserve millennial-scale events and filter inter-annual signal, we decided to apply a first-order low pass filter calibrated with a cut-off frequency of $2 \times 10^{-3}\,yrs^{-1}$ (corresponding to a period of $5000\,yrs$). This is slightly higher than the dominant frequency of the *oscillating simulations* in order not to lose the

information contained in the smaller secondary peaks, mainly observed in *17.8k*. This cut-off frequency, and consequently the filters, are the same for every simulation. The resulting filtered signals are shown by Figure 4*b*.

Compared to the NGRIP temperatures running mean series of Figure 3*c*, Figure 4*b* provides a clearer view of the main features of our time series and neither the periodicity of the signals nor the range of temperatures are significantly altered. Nonetheless, we still note a smoothing during sharper climate changes, where some information contained in higher frequencies may have been obscured by the processing. For example, we do not observe the overshoots at the onset of some warm phases in the filtered signals, and the most extreme warming/cooling rates are also damped.

This spectral analysis is useful for quantitatively assessing *oscillating simulations* with dominant frequencies around a thousand years, but fall short of providing useful information for lower dominant frequencies. For instance, the algorithm does not capture the longer periodicity (of a few thousand years) of *18.2k*. This is because Fourier transforms require a sufficient number of cycles to compute robustly. Hence, our algorithm does not have enough material to establish either way whether the *18.2k* simulation is slowly oscillating, or showing other behaviour such as a complex permanent recovery. Similarly, but more extreme, the absence of a periodic signal in the *warm simulations* prevents the Fourier analysis from being correctly handled, and their responses were therefore not included in this analysis.

For all the stated reasons, we emphasise that it is not appropriate to use the frequency analysis alone to understand our simulations. Instead, we utilise such an approach to

complement the running-mean analysis, contributing an objective quantification of cyclical behaviour to identify oscillations, determine the main frequencies of the millennial-scale variability, and isolate the typical features within our experiments. It also helps to clarify the dynamics of the simulations, which is useful for understanding the behaviours depicted by Figure 6.

S6. Definition of warm and cold composite modes

In order to accurately characterise the simulations in this study, it is useful to be able to analyse aggregate features of the cold and warm climate modes, e.g. as presented in Figures 5. The intricate climate response of the meltwater simulations makes it difficult to adopt an objective definition that is commonly applicable to all simulations of cold and warm modes. A simple approach could be to define a fixed period of time before, after or spanning either side of the coldest/warmest points of the time series. However, this relatively unintelligent algorithm would be heavily susceptible to biases. For example, the warm modes could be biased towards the overshoot during the recovery phase, and the cold modes by the initial transition to a weak AMOC stage. Trying to widen the time spans to avoid this would result in the inclusion of the transition times. A further consideration is that the results need to be consistent between the NGRIP temperatures and the AMOC index time series despite the small lag between the two.

In light of these remarks, six different methods were tested to design the optimal algorithm for identifying the composite data for the cold and warm modes in our simulations, as depicted in Figures S6 and S7. *Method 1* defines the warm and cold modes as the highest and lowest thirds of the 30-year running mean AMOC index time series. *Method 1b* is similar, only it defines the warm and cold modes on the *filtered* time series of the AMOC index. *Method 2* defines the warm and cold modes as the highest and lowest thirds of the 30-year running mean NGRIP temperature time series. *Method 3* defines the warm and cold modes as the highest and lowest quarters of the 30-year running mean AMOC index time series, excluding the first 1000 years for all experiments except *21.5k* and *21k*

to define the quarters; *20.7k*, *19.4k*, *18.2k* and *17.8k* generally show better consistency after the first 1000 years, excluding their adjustment to the initial meltwater perturbation, which has a strong early impact in these simulations. In *Method 4*, we manually defined the warm and cold limits for each simulation to visually fit what looks like a warm or cold period from the 30-year running mean AMOC index time series. *Method 5* defines the warm modes as the 150 year period centred around the maximum of the filtered AMOC time series and the cold modes as the 150 year period centred around the minimum of the AMOC time series. The maximum and minimum have to be spaced 500 years apart and in the highest/lowest thirds and concave/convex for warm/cold modes.

Comparing the effects of each algorithm on the zonal mean anomalies in Figure S8, we observe consistent behaviours during cold modes and slightly more variability in warm modes despite showing similar zonal mean patterns. *Method 3* returns a stronger AMOC in both cold and warm modes of the oscillating and slow-recovery simulations, with the lowest sea ice cover in warm modes. *Method 2* also tends to simulate warmer weak modes of the oscillating and warm experiments. *Method 1* and *Method 5*'s definition of warm modes is too broad in the warm simulations, leading to 1°C cooling of the warm modes. A significant amount of the transition times in cold modes are included in *Method 1* and *Method 3*. Finally, we do not recommend using the filtered time series for non-oscillating simulations as they create artefacts in the NGRIP time series that affect the modes-selection algorithm, which rules out methods Method 1b and *Method 5* from being useful.

Method 4 is the only approach not to present any strong irregularities in the composite warm/cold modes. Although it relies on a visual identification, which could induce bias, the results always rank within the mean behaviour in zonal mean anomalies. The method is simple, but provides the required information needed for the analysis. It is the algorithm that best filters-out the transition periods between the cold and warm phases, and it has the advantage of being easily adaptable and applied to all six simulations. It is, therefore, the algorithm we adopted for this study.

We note that when the amplitude range is small compared to the running mean variability, such as in *21.5k*, some time slices may end up being assigned to the wrong mode by the chosen categorisation method (*Method 4*). Nonetheless, this is infrequent and easy enough to identify (e.g. in Figures 5*g* and 5*n*); thus we can identify that it does not have a significant impact on the presented results.

S7. Intertropical Convergence Zone (ITCZ) index

The Intertropical Convergence Zone (ITCZ) index (Figure 3) was inspired by the work of (Braconnot et al., 2007) and Singarayer, Valdes, and Roberts (2017) and corresponds to the mean northern limit of the ITCZ. It was calculated following equation S3, where $lat(pr_{max})$ is the latitude of the maximum zonally averaged precipitation, pr ($kg\,m^{-2}\,s^{-1}$). Compared to Singarayer et al. (2017), we computed the mean latitude instead of the maximum latitude of the rainbelt to gain a better view of the global displacement of the ITCZ.

$$ITCZ_{index} = mean(\frac{\sum_{y=lat(pr_{max})}^{35°N} pr(lon,y)lat(y)}{\sum_{y=lat(pr_{max})}^{35°N} lat(y)}) \tag{S3}$$

S8. Locating the centre of mass

The lontitude and latitude of the centre of mass of a value $V(lon, lat)$ (used in section 6 and Figure 6) is defined in equation S4. For the sake of simplicity, the volume of each grid cell was not considered in this definition.

$$[lon_{COM}, lat_{COM}]_V = \frac{\sum_{i,j} V(i,j)[lon(i), lat(j)]}{\sum_{i,j} V(i,j)} \tag{S4}$$

C1. Caption for figure S2

a. Meltwater discharge history over the early deglaciation and its distribution over the main regions defined in panel *b*. This plot incorporates the 200-years smoothing described in section S2). Vertical bars represent the time steps chosen for calculating each constant meltwater-forcing snapshot (see section 2.2, and Table 1). *b.* Map of ice meltwater collection and spreading areas. Each individual box corresponds to a freshwater collection area, redistributed to the corresponding spreading areas (within the same box) indicated by the bold contours. Seven main regions were defined for the presented analysis, as labelled on the right (colours). Note that these regions do not correspond to individual regions but rather to clusters of spreading areas. The colour coding matches panel *a*. *c.* Ice sheet meltwater discharge snapshot used for each perturbed meltwater simulation. The names and colours of the simulations correspond to the snapshot time on panel *b*. The colour coding of each simulation matches figures in the main text. Please note the logarithmic scale.

C2. Caption for figure S6

Depiction of the constituent data (here, showing the AMOC index; max Atlantic overturning circulation at 26.5° N) for the warm and cold climate phases arising from the different methods for creating the composite warm and cold modes analysed in the main article (introduced in section 4). Panels *a*, *c*, *d* and *e* used 30-year running-mean of the AMOC index time series. Panels *b* and *f* used the filtered AMOC index time series as described in section S5. See Section S6 text for the detail of the different methods.

C3. Caption for figure S7

Depiction of the constituent data (here, showing the NGRIP surface air temperature, 42.32° W, 75.01° N) for the warm and cold climate phases arising from the different methods for creating the composite warm and cold modes analysed in the main article (introduced in section 4). Panels *a*, *c*, *d* and *e* show the 30-year running-mean of the NGRIP temperature time series. Panels *b* and *f* show the filtered NGRIP temperature time series as described in section S5. See S6 text for the detail of the different methods.

C4. Caption for figure S8

Composite warm and cold modes mean zonal anomalies between the meltwater simulations and the reference state in the Atlantic (70° W – 10° E). Solid lines are cold modes and dashed lines are warm modes, which have been compiled using the five methods described in the text (section S6). Panels show the zonally averaged surface air temperature, sea surface temperature, mixed layer depth, winter sea ice concentration, summer sea ice and maximum overturning circulation flow over the water column for the different methods and applied to three simulations corresponding to the three different clusters identified in section 4. Figures S6 and S7 highlight the constituent data for the warm and cold modes identified by each method.

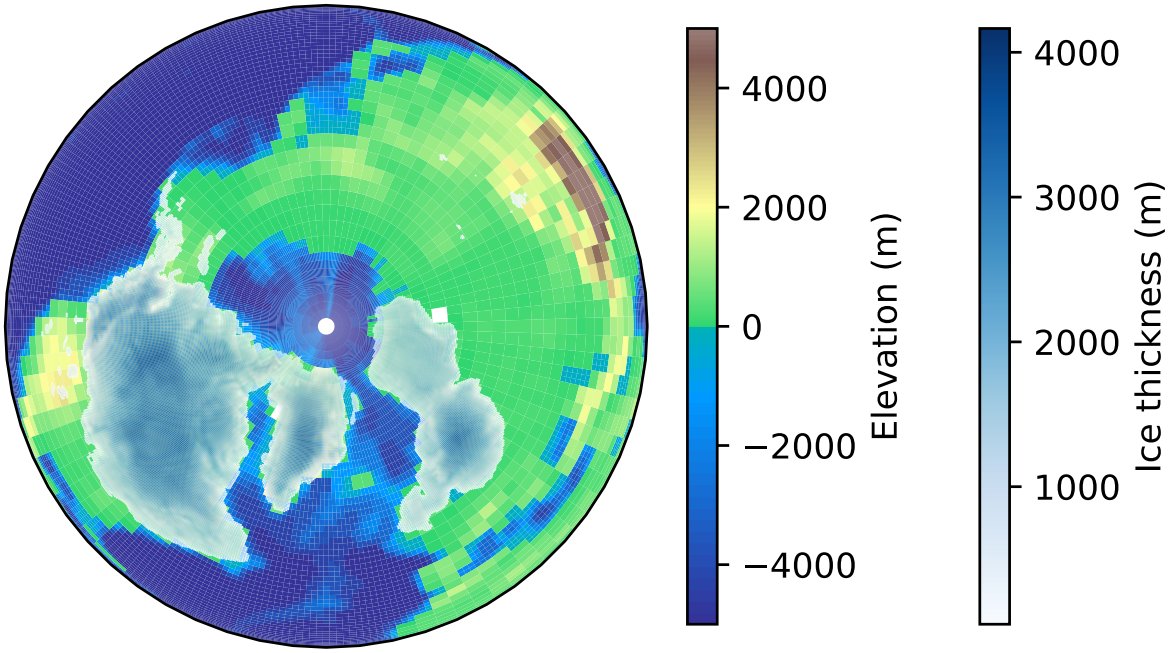

Figure S1. Orography, bathymetry, land sea mask and ice sheet elevation boundary conditions in the Arctic region. Ice sheets were reconstructed from GLAC-1D at 21 ka BP. Terrestrial ice is shown where it is thicker than 50 m.

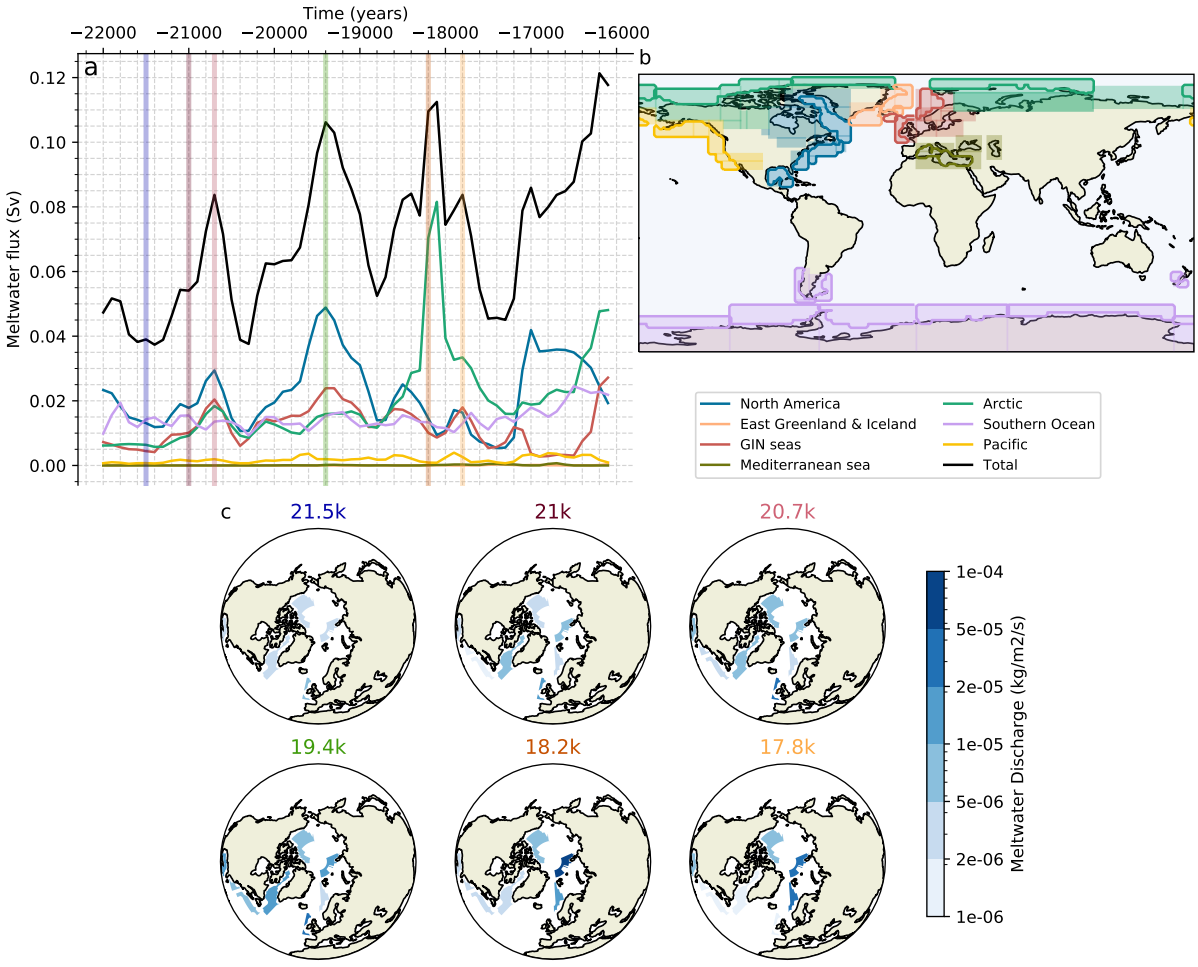

Figure S2. See Caption C1.

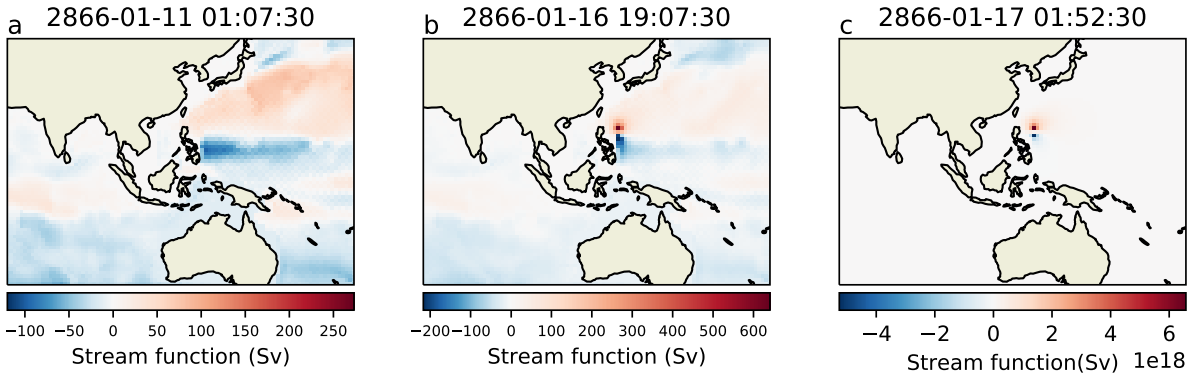

Figure S3. *a.* Barotropic stream function in *CTRL* during the simulated week before numerical instability causes the model to crash, *b.* at the development of the instability and *c.* at the time of the crash. Note the difference in scales.

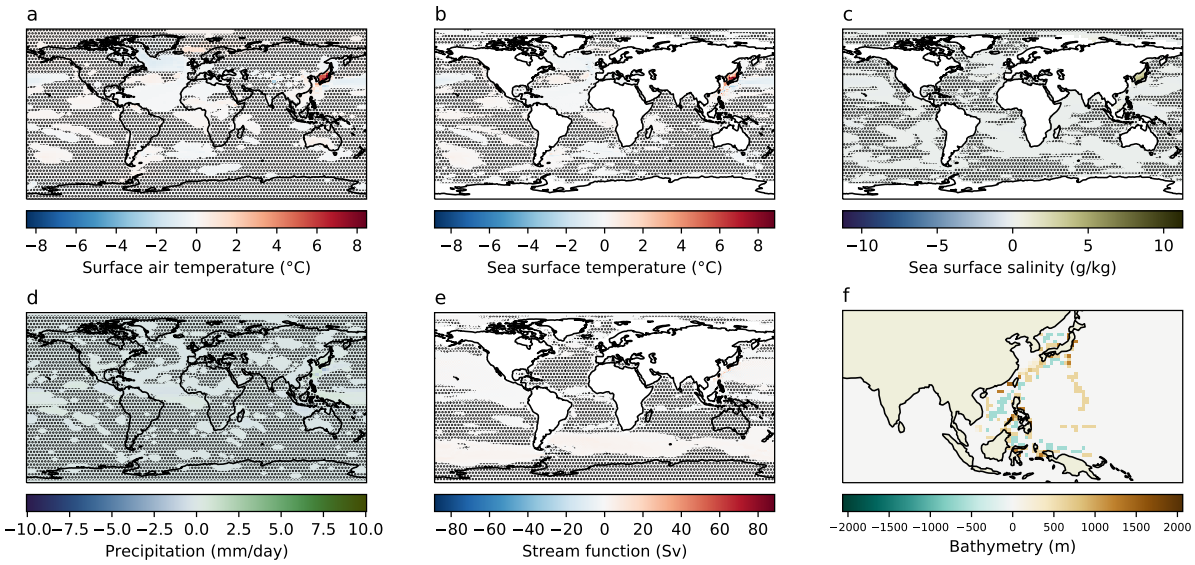

Figure S4. *a.*Changes in surface air temperature, *b.* sea surface temperature, *c.* surface salinity, *d.* precipitation, *e.* stream function and *f.* bathymetry in *CTRL* after applying the smoothing algorithm (using the pre/post-smoothing time windows defined in Figure S5). Hatching is applied where values are considered statistically insignificant using a student t-test with a p-value of 0.1 .

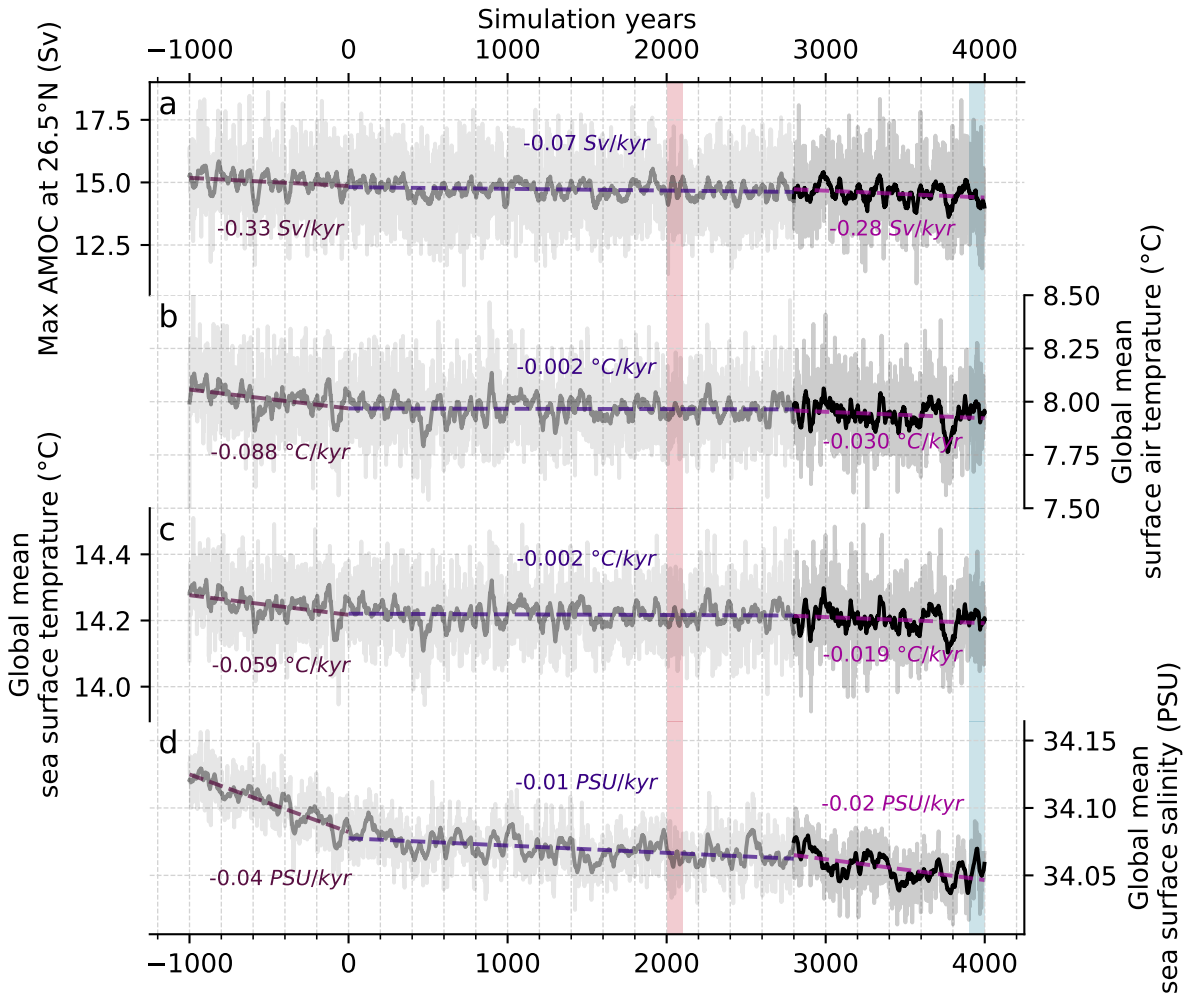

Figure S5. *a.* AMOC index, *b.* global mean surface air temperature, *c.* sea surface temperature and *d.* sea surface salinity trends in the *CTRL* simulation. Light/dark colours correspond to before/after the application of the smoothing algorithm, respectively. The last thousand years of spin-up are shown at the start of the run, for context. The drifts (purple) are calculated from linear regression of the time series before (darker purple) and after (lighter purple) the restart of the run and during the last thousand years of spin-up (medium purple). Red and blue shading highlights the pre and post smoothing phases used in Figure S4, respectively

.

March 24, 2022, 8:41pm

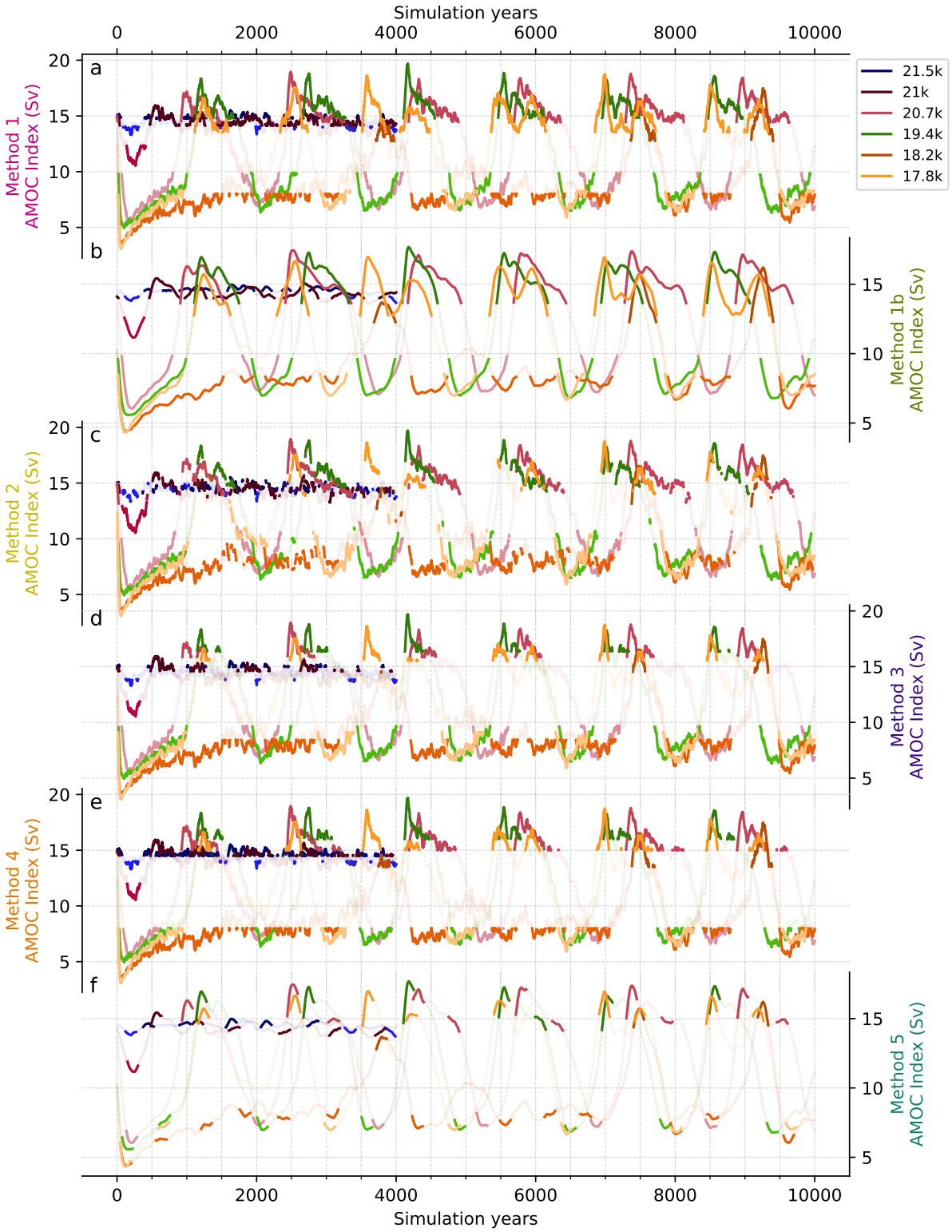

Figure S6. See Caption C2.

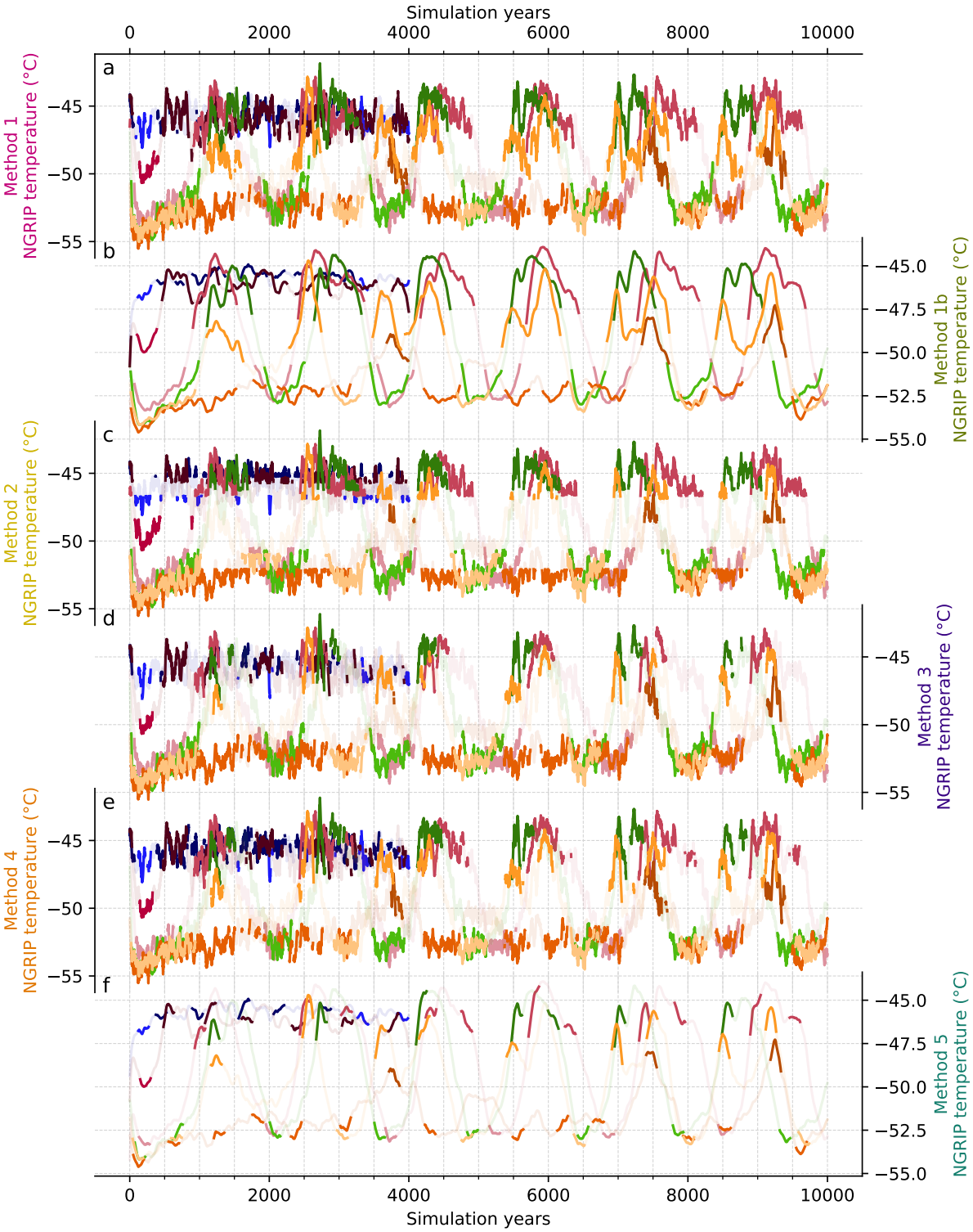

Figure S7. See Caption C3.

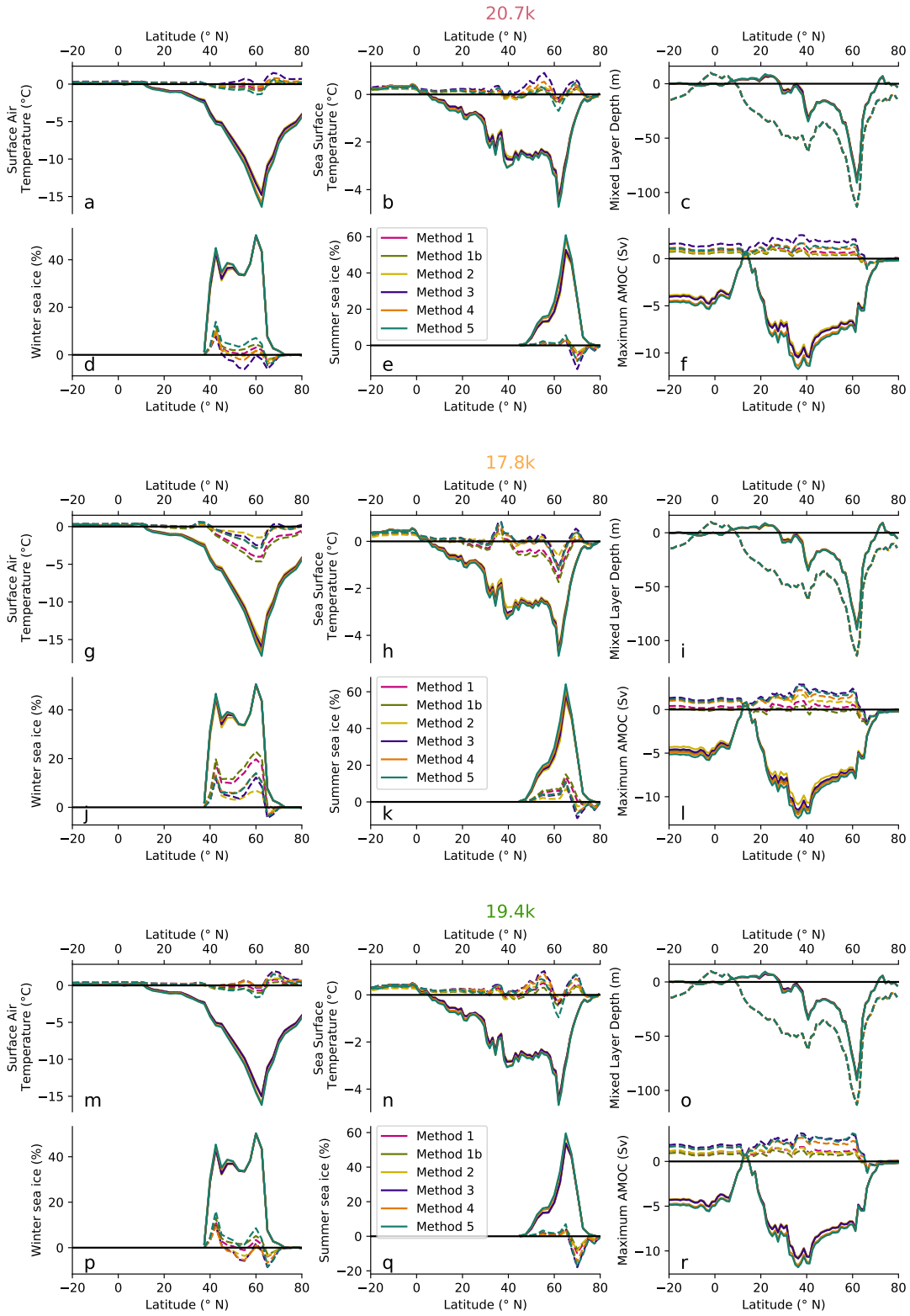

Figure S8. See Caption C4.

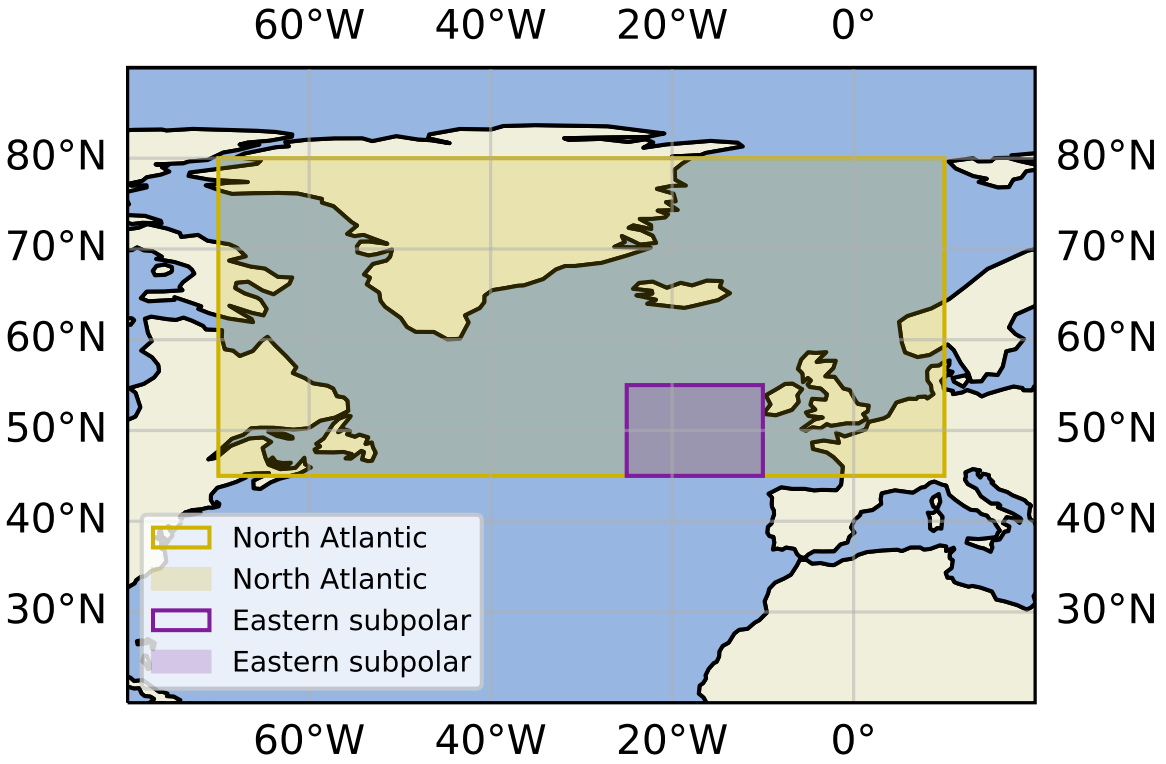

Figure S9. Definition of North Atlantic zones used for the analysis summarised by Figure 6.

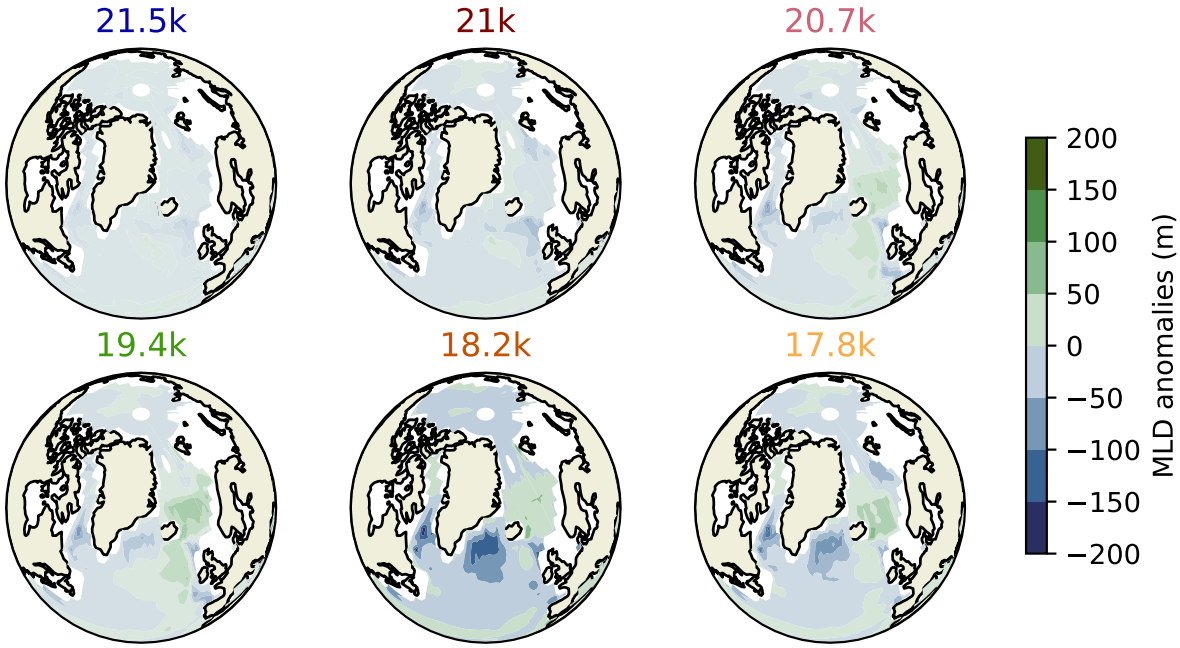

Figure S10. Mean annual mixed layer depth anomalies between the meltwater simulations and *CTRL* over the composite warm modes.

References

Bereiter, B., Eggleston, S., Schmitt, J., Nehrbass-Ahles, C., Stocker, T. F., Fischer, H., ... Chappellaz, J. (2015). Revision of the EPICA Dome C CO2 record from 800 to 600 kyr before present. *Geophysical Research Letters*, *42*(2), 542–549. Retrieved 2020-03-10, from https://agupubs.onlinelibrary.wiley.com/doi/abs/10.1002/2014GL061957 (_eprint: https://agupubs.onlinelibrary.wiley.com/doi/pdf/10.1002/2014GL061957) doi: 10.1002/2014GL061957

Braconnot, P., Otto-Bliesner, B., Harrison, S., Joussaume, S., Peterchmitt, J.-Y., Abe-Ouchi, A., ... Zhao, Y. (2007, June). Results of PMIP2 coupled simulations of the Mid-Holocene and Last Glacial Maximum – Part 2: feedbacks with emphasis on the location of the ITCZ and mid- and high latitudes heat budget. *Climate of the Past*, *3*(2), 279–296. Retrieved 2022-02-02, from https://cp.copernicus.org/articles/3/279/2007/ (Publisher: Copernicus GmbH) doi: 10.5194/cp-3-279-2007

Briggs, R. D., Pollard, D., & Tarasov, L. (2014, November). A data-constrained large ensemble analysis of Antarctic evolution since the Eemian. *Quaternary Science Reviews*, *103*, 91–115. Retrieved 2020-03-08, from http://www.sciencedirect.com/science/article/pii/S0277379114003448 doi: 10.1016/j.quascirev.2014.09.003

Bryan, K., & Cox, M. D. (1972, October). An Approximate Equation of State for Numerical Models of Ocean Circulation. *Journal of Physical Oceanography*, *2*(4), 510–514. Retrieved 2021-09-07, from https://journals.ametsoc.org/view/journals/phoc/2/4/1520-0485_1972_002_0510_aaeosf_2_0_co_2.xml doi: 10.1175/1520-0485(1972)002⟨0510:AAEOSF⟩2.0.CO;2

Dentith, J. E., Ivanovic, R. F., Gregoire, L. J., Tindall, J. C., & Smith, R. S. (2019, February). Ocean circulation drifts in multi-millennial climate simulations: the role of salinity corrections and climate feedbacks. *Climate Dynamics*, *52*(3), 1761–1781. Retrieved 2021-10-28, from https://doi.org/10.1007/s00382-018-4243-y doi: 10.1007/s00382-018-4243-y

Fofonoff, N. P. (1985). Physical properties of seawater: A new salinity scale and equation of state for seawater. *Journal of Geophysical Research: Oceans*, *90*(C2), 3332–3342. Retrieved 2021-09-07, from https://agupubs.onlinelibrary.wiley.com/doi/abs/10.1029/JC090iC02p03332 doi: 10.1029/JC090iC02p03332

Fofonoff, N. P., & Millard Jr, R. C. (1983). Algorithms for the computation of fundamental properties of seawater. *UNESCO Technical Papers in Marine Sciences*. Retrieved 2021-09-07, from https://repository.oceanbestpractices.org/handle/11329/109 doi: 10.25607/OBP-1450

Gordon, C., Cooper, C., Senior, C. A., Banks, H., Gregory, J. M., Johns, T. C., ... Wood, R. A. (2000, February). The simulation of SST, sea ice extents and ocean heat transports in a version of the Hadley Centre coupled model without flux adjustments. *Climate Dynamics*, *16*(2), 147–168. Retrieved 2020-07-09, from https://doi.org/10.1007/s003820050010 doi: 10.1007/s003820050010

Ivanovic, R. F., Gregoire, L. J., Burke, A., Wickert, A. D., Valdes, P. J., Ng, H. C., ... Dentith, J. E. (2018). Acceleration of Northern Ice Sheet Melt Induces AMOC Slowdown and Northern Cooling in Simulations of the Early Last Deglaciation. *Paleoceanography and Paleoclimatology*, *33*(7), 807–824. Retrieved 2019-10-02, from https://agupubs.onlinelibrary.wiley.com/doi/abs/10.1029/2017PA003308 doi: 10.1029/2017PA003308

Ivanovic, R. F., Gregoire, L. J., Kageyama, M., Roche, D. M., Valdes, P. J., Burke, A., ... Tarasov, L. (2016, July). Transient climate simulations of the deglaciation 21–9 thousand years before present (version 1) – PMIP4 Core experiment design and boundary conditions. *Geoscientific Model Development*, *9*(7), 2563–2587. Retrieved 2020-02-20, from https://www.geosci-model-dev.net/9/2563/2016/ doi: https://doi.org/10.5194/gmd-9-2563-2016

Ivanovic, R. F., Gregoire, L. J., Wickert, A. D., & Burke, A. (2018). Climatic Effect of Antarctic Meltwater Overwhelmed by Concurrent Northern Hemispheric Melt. *Geophysical Research Letters*, *45*(11), 5681–5689. Retrieved 2021-04-05, from https://agupubs.onlinelibrary.wiley.com/doi/abs/10.1029/2018GL077623 (_eprint: https://agupubs.onlinelibrary.wiley.com/doi/pdf/10.1029/2018GL077623) doi: https://doi.org/10.1029/2018GL077623

Ivanovic, R. F., Gregoire, L. J., Wickert, A. D., Valdes, P. J., & Burke, A. (2017). Collapse of the North American ice saddle 14,500 years ago caused widespread cooling and reduced ocean overturning circulation. *Geophysical Research Letters*, *44*(1), 383–392. Retrieved 2020-07-09, from https://agupubs.onlinelibrary.wiley.com/doi/abs/10.1002/2016GL071849 (_eprint: https://agupubs.onlinelibrary.wiley.com/doi/pdf/10.1002/2016GL071849) doi: 10.1002/2016GL071849

Kageyama, M., Albani, S., Braconnot, P., Harrison, S. P., Hopcroft, P. O., Ivanovic, R. F., ... Zheng, W. (2017, November). The PMIP4 contribution to CMIP6 – Part 4: Scientific objectives and experimental design of the PMIP4-CMIP6 Last Glacial Maximum experiments and PMIP4 sensitivity experiments. *Geoscientific Model Development*, *10*(11), 4035–4055.

Retrieved 2020-02-20, from https://www.geosci-model-dev.net/10/4035/2017/ doi: https://doi.org/10.5194/gmd-10-4035-2017

Loulergue, L., Schilt, A., Spahni, R., Masson-Delmotte, V., Blunier, T., Lemieux, B., ... Chappellaz, J. (2008, May). Orbital and millennial-scale features of atmospheric CH 4 over the past 800,000 years. *Nature*, *453*(7193), 383–386. Retrieved 2020-03-10, from https://www.nature.com/articles/nature06950 (Number: 7193 Publisher: Nature Publishing Group) doi: 10.1038/nature06950

Schilt, A., Baumgartner, M., Schwander, J., Buiron, D., Capron, E., Chappellaz, J., ... Stocker, T. F. (2010, November). Atmospheric nitrous oxide during the last 140,000years. *Earth and Planetary Science Letters*, *300*(1), 33–43. Retrieved 2020-03-10, from http://www.sciencedirect.com/science/article/pii/S0012821X10006023 doi: 10.1016/j.epsl.2010.09.027

Singarayer, J. S., Valdes, P. J., & Roberts, W. H. G. (2017, August). Ocean dominated expansion and contraction of the late Quaternary tropical rainbelt. *Scientific Reports*, *7*(1), 9382. Retrieved 2022-01-21, from https://www.nature.com/articles/s41598-017-09816-8 doi: 10.1038/s41598-017-09816-8

Tarasov, L., Dyke, A. S., Neal, R. M., & Peltier, W. R. (2012, January). A data-calibrated distribution of deglacial chronologies for the North American ice complex from glaciological modeling. *Earth and Planetary Science Letters*, *315-316*, 30–40. Retrieved 2020-03-08, from http://www.sciencedirect.com/science/article/pii/S0012821X11005243 doi: 10.1016/j.epsl.2011.09.010

Tarasov, L., & Peltier, R. W. (2002, July). Greenland glacial history and local geodynamic

consequences. *Geophysical Journal International*, *150*(1), 198–229. Retrieved 2020-03-10, from https://academic.oup.com/gji/article/150/1/198/591943 (Publisher: Oxford Academic) doi: 10.1046/j.1365-246X.2002.01702.x